Article

Long-Range Magnetic Ordering in Iron Jarosites Prepared by Redox-Based Hydrothermal Methods

Bart M. Bartlett, and Daniel G. Nocera

J. Am. Chem. Soc., **2005**, 127 (25), 8985-8993• DOI: 10.1021/ja050205d • Publication Date (Web): 03 June 2005

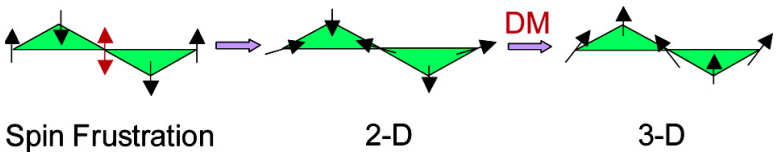

More About This Article

Additional resources and features associated with this article are available within the HTML version:

- Supporting Information
- Links to the 15 articles that cite this article, as of the time of this article download
- Access to high resolution figures
- Links to articles and content related to this article
- Copyright permission to reproduce figures and/or text from this article

View the Full Text HTML

J|A|C|S
ARTICLES
Published on Web 06/03/2005

Long-Range Magnetic Ordering in Iron Jarosites Prepared by Redox-Based Hydrothermal Methods

Bart M. Bartlett and Daniel G. Nocera*

Contribution from the Department of Chemistry, 6-335, Massachusetts Institute of Technology, 77 Massachusetts Avenue, Cambridge, Massachusetts 02139

Received January 12, 2005; E-mail: nocera@mit.edu

Abstract: The iron jarosites, plumbojarosite, $Pb_{0.5}Fe_3(OH)_6(SO_4)_2$, argentojarosite, $AgFe_3(OH)_6(SO_4)_2$, and thallium jarosite, $TlFe_3(OH)_6(SO_4)_2$, along with the selenate-capped jarosite analogues of potassium, $KFe_3(OH)_6(SeO_4)_2$, and rubidium, $RbFe_3(OH)_6(SeO_4)_2$, have been prepared in their analytically pure forms by employing redox-based hydrothermal methods. The crystal structures of these materials have been determined, and all are found to be essentially isostructrual including $Pb_{0.5}Fe_3(OH)_6(SO_4)_2$, which is distinct from the structure reported for naturally mined samples. All iron jarosites show long-range order (LRO), signified by a sharp transition temperature, T_N, which falls in the narrow temperature range of 61.4 ± 5 K. The mechanism responsible for this ordering has been established by examining magnetostructural correlations for the jarosites possessing various interlayer cation and capping groups. We show that all magnetic properties of jarosites, including LRO, find their origin in the basic magnetic unit, the intralayer $Fe_3(\mu\text{-}OH)_3$ triangle. Field-dependent magnetization experiments are consistent with the antiferromagnetic stacking of an out of plane moment developed from spin canting within $Fe_3(\mu\text{-}OH)_3$ triangles. Together with the previously reported $AFe_3(OH)_6(SO_4)_2$ ($A = Na^+$, K^+, Rb^+ and NH_4^+) jarosites, these compounds provide a framework for probing magnetic ordering in a spin frustrated lattice of the largest series of isoelectronic and isostructural kagomé systems yet discovered.

Introduction

The spin ground state of highly correlated electron systems may remain magnetically disordered in lattices exhibiting high degeneracy. For these cases, fluctuations among an exceptionally large number of different spin configurations at the same energy are sufficient to suppress long-range order (LRO).[1−5] The situation is especially prevalent for geometrically frustrated lattices bearing antiferromagnetically coupled spins because the connectivity of the lattice prevents the spins from achieving a configuration that minimizes the magnetic exchange energy.[1,6] The kagomé lattice, formed of corner sharing triangles, is the most highly geometrically frustrated two-dimensional lattice. For classical spins with antiferromagnetic exchange, the ordered state shown in Figure 1 is but one of an infinite family of degenerate ground states. For quantum spins, the situation is even more complex and various theoretical treatments predict a ground state that remains quantum disordered at $T = 0$.[7−10]

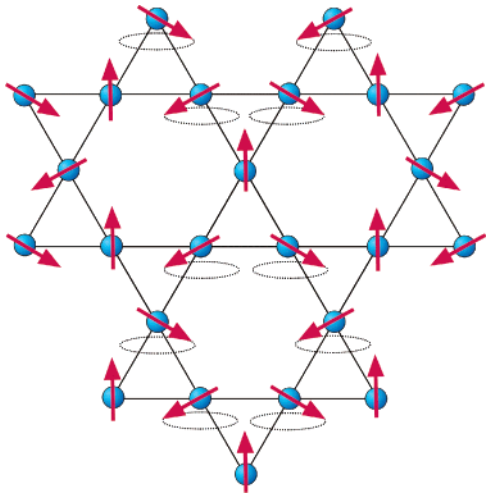

Figure 1. The kagomé lattice with spins in one possible ground-state configuration. Note that the spins on a hexagon can be rotated out of the plane about the dotted ellipse without changing the energy, thus giving rise to an infinite number of degenerate ground states.

Of the various known kagomé lattices, that of the jarosite family of compounds has long been regarded as a principal model for studying spin frustration.[1,5,6,8,11−14] This alunite

(1) Ramirez, A. P. *Annu. Rev. Mater. Sci.* **1994**, *24*, 453−80.
(2) Lhuillier, C. Misguich, G. *Lect. Notes Phys.* **2001**, *595*, 161−90.
(3) Shender, E. F.; Holdsworth, P. C. W. In *Fluctuations and Order*; Millonas, M., Ed., Springer-Verlag: Berlin, 1996; p 259.
(4) Reimers, J. N.; Berlinsky, A. J. *Phys. Rev. B* **1993**, *48*, 9539−54.
(5) Chalker, J. T.; Holdsworth, P. C. W.; Shender, E. F. *Phys. Rev. Lett.* **1992**, *68*, 855−8.
(6) Greedan, J. E. *J. Mater. Chem.* **2001**, 11, 37−53.
(7) Koretsune, T.; Ogata, M. *Phys. Rev. Lett.* **2002**, *89*, 116401/1−4.
(8) Harris, A. B.; Kallin, C.; Berlinsky, A. J. *Phys. Rev. B* **1992**, *45*, 2899−919.
(9) Chalker, J. T.; Eastmond, J. F. G. *Phys. Rev. B* **1992**, *46*, 14201−4.
(10) Sindzingre, S.; Misguich, G.; Lhuillier, C.; Bernu, B.; Pierre, L.; Waldtmann, C.; Everts, H. U. *Phys. Rev. Lett.* **2000**, *84*, 2953−6.
(11) Ramirez, A. P. In *Handbook on Magnetic Materials*; Busch, K. J. H, Ed.; Elsevier Science: Amsterdam, 2001; Vol. 13, pp 423−520.
(12) Sachdev, S. *Phys. Rev. B* **1992**, *45*, 12377−96.
(13) Ritchey, I.; Chandra, P.; Coleman, O. *Phys. Rev. B* **1993**, *47*, 15342−5.
(14) Wills, A. S.; Harrison, A. *J. Chem. Soc., Faraday Trans.* **1996**, *92*, 2161−6.

superfamily subgroup, based on the $KFe_3(OH)_6(SO_4)_2$ parent, is composed exclusively of kagomé layers formed from $Fe^{III}_3(\mu\text{-}OH)_3$ triangles.[15] The alternate faces of neighboring triangles are capped by the sulfate dianion, with the potassium cation sitting in an icosahedral site opposite the sulfate caps. Even though jarosites should not order at any nonzero temperature owing to the infinite number of degenerate ground states, LRO is observed.[14,16] For these compounds, like all real magnetic materials, terms contained in the interaction Hamiltonian beyond isotropic Heisenberg exchange engender LRO at nonzero temperatures arising from weak interplanar coupling, spin anisotropy and/or anisotropic exchange or lattice disorder. The latter ordering mechanism is particularly relevant to jarosites because the monovalent A^+ cations are susceptible to replacement by hydronium ions and/or the coverage of the M^{3+} magnetic lattice sites is incomplete.[17,18] The presence of these site defects has been most commonly cited as the reason for the observed LRO in jarosites.[14,18] Notwithstanding, we have developed a redox-based hydrothermal method to afford single crystalline and stoichiometrically pure (i.e., complete lattice coverage) Fe^{3+} jarosites containing the alkali interlayer cations Na^+, K^+, and Rb^+ and LRO is observed.[19] The presence of an antiferromagnetic transition in stoichiometrically pure jarosites implies the existence of some intrinsic mechanism for three-dimensional magnetic ordering in the kagomé lattice of layered jarosite compounds.

Theory predicts that LRO in jarosites may arise from spin anisotropy developed by the Dzyaloshinsky−Moriya (DM) interaction,[20] which induces a moment by canting spins slightly out of the plane. Within the chemistry community, the DM interaction has been sought in molecular trimers that possess a spin-frustrated antiferromagnetic ground state.[21−27] However, geometric distortion of the molecular triangle tends to obscure the direct observation of the DM interaction.[25] As we show here, distortion of the triangles is not prevalent when the triangles are catenated into an extended 2-D kagomé lattice thus allowing us to incisively probe the DM interaction and its role in establishing LRO in jarosites. By employing the redox-based hydrothermal method, an extensive series of jarosites have been prepared featuring different cations and anionic capping groups, $AFe_3(OH)_6(TO_4)_2$ ($A = {}^1/_2Pb^{2+}$, Ag^+, Tl^+ and $TO_4 = SO_4^{2-}$; $A = K^+$ and Rb^+ and $TO_4 = SeO_4^{2-}$). Together with the previously reported $AFe_3(OH)_6(SO_4)_2$ ($A = Na^+$, K^+, Rb^+ and NH_4^+) jarosites, these compounds provide a framework for probing magnetic ordering in a spin frustrated lattice of the largest series of isoelectronic and isostructural kagomé systems yet discovered. We provide direct evidence that LRO in jarosites finds its origins in the DM interaction within $Fe^{III}_3(\mu\text{-}OH)_3$ triangular subunits of the kagomé lattice.

Experimental Section

General Procedures. All chemicals of reagent or analytical grade were obtained from Aldrich, and they were used without purification. Hydrothermal reactions were carried out in Teflon-lined pressure vessels, which were purchased from Parr Instruments. A Fisher Isotemp programmable oven with forced-air circulation was used to obtain the desired temperature profiles for hydrothermal reactions. Chemical analyses were conducted by the H. Kolbe Mikroanalytisches Laboratorium.

Synthesis of $Pb_{0.5}Fe_3(OH)_6(SO_4)_2$. A 23-mL Teflon liner was charged with 0.168 g of 2.0 mm iron wire (3.00 mmol). In a separate, small beaker, 0.199 g of $Pb(NO_3)_2$ (0.600 mmol) was dissolved in 10 mL of deionized water. Into this solution, 0.50 mL of concentrated sulfuric acid (9.0 mmol) was added via Mohr pipet. $PbSO_4$ was observed to precipitate after which 0.58 mL of concentrated HNO_3 (9.0 mmol) was added to the mixture via Mohr pipet; the resulting mixture was stirred for 15 min. The beaker mixture was poured into the Teflon liner, including several backwashings to transfer all of the lead sulfate precipitate. The liner was sealed and placed into a steel hydrothermal bomb in an Aldrich Atmosbag under an atmosphere of oxygen. The tightened bomb was heated at a rate of 5 °C/min to 210 °C, which was maintained for 72 h. The oven was cooled to room temperature at a rate of 0.1 °C/min. A yellow-orange crystalline powder was isolated from the bottom of the liner; it was washed with deionized water and then 150 mL of a 1:1 HNO_3:H_2O mixture which was heated to 100 °C in order to remove the residual lead sulfate byproduct. The powder was then washed a second time with deionized water and dried in air. Yield: 0.302 g (53.4% based on starting iron). The product was determined to be plumbojarosite, $Pb_{0.5}Fe_3(OH)_6(SO_4)_2$, by powder X-ray diffraction. Anal. Calcd. for $H_6Pb_{0.5}Fe_3S_2O_{14}$: H, 1.07; Pb, 18.33; Fe, 29.64; S 11.34. Found: H, 1.12; Pb, 18.26; Fe, 29.72; S, 11.41.

Synthesis of $AgFe_3(OH)_6(SO_4)_2$ and $TlFe_3(OH)_6(SO_4)_2$. A 125-mL Teflon liner was charged with 0.563 g of 2.0 mm iron wire (10.1 mmol). In a separate beaker, the nitrate salt of the interlayer cation (1.711 g of silver nitrate (10.07 mmol), or 2.662 g of thallium nitrate (9.99 mmol)) was dissolved in 50 mL of deionized water. Into this solution, 2.2 mL of concentrated sulfuric acid (40 mmol) was added via Mohr pipet, and the resulting solution was allowed to stir for 15 min. The beaker solution was poured into the Teflon liner, which was then capped and placed into a steel hydrothermal bomb under an atmosphere of oxygen using an Aldrich Atmosbag. The tightened bomb was heated at a rate of 5 °C/min to 210 °C, which was maintained for 72 h. The oven was then cooled to room temperature at a rate of 0.1 °C/min. A yellow-orange crystalline powder was isolated from the walls and the bottom of the Teflon liner, and the product was washed with deionized water and dried in air. The powder was identified by powder X-ray diffraction. Yield: 1.697 g of $AgFe_3(OH)_6(SO_4)_2$ (88.5% based on starting Fe) and 1.466 g of $TlFe_3(OH)_6(SO_4)_2$ (66.1% based on starting Fe). Anal. Calcd. for $H_6AgFe_3S_2O_{14}$: H, 1.06; Ag, 18.94; Fe, 29.41; S, 11.26. Found: H, 1.12; Ag, 18.82; Fe, 29.50; S, 11.35. Anal. Calcd. for $H_6TlFe_3S_2O_{14}$: H, 0.91; Tl, 30.68; Fe, 25.15; S, 9.63. Found: H, 0.92; Tl, 30.44; Fe, 25.17; S, 9.65.

Synthesis of $KFe_3(OH)_6(SeO_4)_2$ and $RbFe_3(OH)_6(SeO_4)_2$. A 23-mL Teflon liner was charged with 0.168 g of 2.0 mm iron wire (3.00 mmol). In a separate, small beaker, the interlayer cation salt (0.660 g of potassium selenate (2.98 mmol), or 0.299 g rubidium nitrate (2.03 mmol)) was dissolved in 10 mL of deionized water. Into this solution, 0.37 mL of selenic acid (6.0 mmol) and 0.58 mL of concentrated nitric acid (9.0 mmol) were added via Mohr pipet for the potassium analogue,

(15) Jambor, J. L. *Can. Mineral.* **1999**, *37*, 1323−41.
(16) Inami, T.; Nishiyama, M.; Maegawa, S.; Oka, Y. *Phys. Rev. B* **2000**, *61*, 12181−6.
(17) Grohol, D.; Nocera, D. G. *J. Am. Chem. Soc.* **2002**, *124*, 2640−6.
(18) Wills, A. S.; Harrison, A.; Ritter, C.; Smith, R. I. *Phys. Rev. B* **2000**, *61*, 6156−69.
(19) Grohol, D.; Nocera, D. G.; Papoutsakis, D. *Phys. Rev. B* **2003**, *67*, 064401/1−13.
(20) Elhajal, M. Canals, B. Lacroix, C. *Phys. Rev. B* **2002**, *66*, 014422/1−6.
(21) Tsukerblat, B. S.; Novotortsev, V. M.; Kuyavskaya, B. Ya.; Belinsky, M. I.; Ablov, A. V.; Bazhan, A. N.; Kalinnikov, V. T. *Sov. Phys. JETP Lett.* **1974**, *19*, 277−8.
(22) Tsukerblat, B. S.; Kuyavskaya, B. Ya.; Belinskii, M. I.; Ablov, A. V.; Novotortsev, V. M.; Kalinnikov, V. T. *Theor. Chim. Acta (Berl.)* **1975**, *38*, 131−8.
(23) Cannon, R. D.; White, R. P. *Prog. Inorg. Chem.* **1988**, *36*, 195−298.
(24) Clemente, J. M.; Palii, A. V.; Tsukerblat, B. S.; Georges, R. In *Molecular Magnetism: From Molecular* Assemblies to the Devices; Coronado, E., Delhaes, P., Gatteschi, D., Miller, J. S., Eds.; Kluwer: Dordrecht, 1996; pp 85−104.
(25) Yoon, J.; Mirica, L. M.; Stack, T. D. P.; Solomon, E. I. *J. Am. Chem. Soc.* **2004**, *126*, 12586−95.
(26) Padilla, J.; Gatteschi, D.; Chaudhuri, P. *Inorg. Chim. Acta* **1997**, *260*, 217−20.
(27) Belinsky, M. I. *Inorg. Chem.* **2004**, *43*, 739−46.

Table 1. Structural Refinement Data for Newly Prepared Iron Jarosites

empirical formula	$H_6Pb_{0.5}Fe_3S_2O_{14}$	$H_6AgFe_3S_2O_{14}$	$H_6TlFe_3S_2O_{14}$	$H_6KFe_3Se_2O_{14}$	$H_6RbFe_3Se_2O_{14}$
formula weight	565.32	569.59	666.09	594.59	640.99
crystal system	rhombohedral	rhombohedral	rhombohedral	rhombohedral	rhombohedral
space group	$R\bar{3}m$	$R\bar{3}m$	$R\bar{3}m$	$R\bar{3}m$	$R\bar{3}m$
a (Å)	7.328(2)	7.3300(9)	7.3226(7)	7.3029(9)	7.4022(16)
c (Å)	16.795(6)	16.497(3)	17.610(2)	17.498(3)	17.816(5)
α (deg)	90	90	90	90	90
γ (deg)	120	120	120	120	120
Z	3	3	3	3	3
V (Å^3)	781.1(4)	767.62(19)	817.74(15)	827.6(2)	845.4(4)
ρ_{calcd} (g/cm^3)	3.606	3.696	4.058	3.579	3.777
θ range (deg)	3.45−23.25	3.44−23.27	3.41−23.22	3.39−23.27	3.38−28.47
T (K)	183(2)	183(2)	183(2)	183(2)	100(2)
F(000)	848	825	927	849	301
no. refl. collected	937	1039	1080	1130	5356
no. unique relections	164	161	169	171	293
no. of parameters	34	29	29	29	29
$R1$ ($I > 2\sigma$; all data)	0.0268; 0.0297	0.0255; 0.0259	0.0207; 0.0212	0.0367; 0.0374	0.0156; 0.0162
$wR2$ ($I > 2\sigma$; all data)	0.05381; 0.0552	0.0642; 0.0644	0.0546; 0.0728	0.0781; 0.0786	0.0433; 0.0436
GOF on F^2	1.190	1.224	1.292	1.245	1.116

and 0.19 mL of selenic acid and 0.26 mL of concentrated nitric acid (4.0 mmol) were added for the rubidium analogue. The resulting solution was allowed to stir for 15 min. The beaker solution was poured into the Teflon liner, which was then capped and placed into a steel hydrothermal bomb under an atmosphere of oxygen in an Aldrich Atmosbag. The tightened bomb was heated at a rate of 5 °C/min to 210 °C, which was maintained for 72 h. The oven was then cooled to room temperature at a rate of 0.1 °C/min. This reaction is limited by the passivation of the iron wire, which was physically removed from complete reaction mixtures. A yellow-orange crystalline powder was isolated from the walls and bottom of the Teflon liner, and the product was washed with deionized water and dried in air. The powder was identified by powder X-ray diffraction. Yield: 0.327 g of $KFe_3(OH)_6(SeO_4)_2$ (55.2% based on starting Fe) and 0.112 g of $RbFe_3(OH)_6(SeO_4)_2$ (17.5% based on starting Fe). Anal. Calcd. for $H_6KFe_3Se_2O_{14}$: H, 1.02; K, 6.58; Fe, 28.18; Se, 26.56. Found: H, 0.98; K, 6.48; Fe, 28.24; Se, 26.50. Anal. Calcd. for $H_6RbFe_3Se_2O_{14}$: H, 0.94; Rb, 13.33; Fe, 26.14; Se, 24.64. Found: H, 0.92; Rb, 13.25; Fe, 26.24; Se, 24.71.

X-ray Diffraction. Powder X-ray diffraction patterns were measured using a Rigaku RU300 rotating anode X-ray diffractometer with Cu Kα radiation ($\lambda = 1.5405$ Å), which was wavelength-selected with a single-crystal graphite monochromator. Samples were spread onto a glass slide fixed with double-sided Scotch tape. θ was fixed at 10° and intensity was recorded as a function of 2θ from 5 to 50°. Patterns were indexed with MDI Jade software version 6.0 and references using the JCPDS powder diffraction database.

X-ray diffraction data were collected using a Siemens three-circle single-crystal diffractometer on a SMART platform equipped with a CCD area detector. All data were acquired at −90 °C using Mo Kα radiation ($\lambda = 0.71073$ Å), which was wavelength-selected with a single-crystal graphite monochromator. For each crystal, at least four data sets of 40-s frames were collected over a hemisphere of reciprocal space using ω scans and a −0.3° scan width. The data frames were integrated to *hkl*/intensity, and final unit cells were calculated using the SAINT program. All structures were solved by the Patterson methods and all heavy atoms were refined anisotropically using version 6.1 of the Brüker SHELXTL suite of programs. Details regarding the refined data and cell parameters are provided in Table 1.

Physical Methods. IR spectra were recorded in KBr pellets on a Nicolet Magna-IR 860 spectrometer equipped with a KBr beam splitter and a DTGS detector. For each spectrum, 32 scans were acquired with 4 cm^{-1} resolution over an energy range of 4000−400 cm^{-1}.

Magnetic susceptibilities were determined on powdered samples contained in gelatin capsules using a Quantum Design MPMSR2 Susceptometer over a 5−300 K temperature range at field strengths varying from 0 to 50 kOe. For each dc susceptibility data point, the average of three measurements of 32 scans over a 4 cm scan length was acquired. Data were corrected for core diamagnetism using Pascal's constants. Ac susceptibilities were recorded for each compound under an ac field, $H_{ac} = H_0 \sin(2\pi ft)$ for $H_0 = 3$ Oe and $f = 2$, 20, and 200 Hz.

Magnetization was determined on powdered samples of $RbFe_3(OH)_6(SO_4)_2$ and $Pb_{0.5}Fe_3(OH)_6(SO_4)_2$ using a Quantum Design PPMS Magnetometer over a 5−65 K temperature range at field strengths varying from 0 to 14 T. For each dc data point, the average of 10 extraction magnetometry scans were acquired. Raw magnetization data were corrected for paramagnetic contributions by subtracting the Brillouin function.

Results

Jarosite Synthesis. Until recently, jarosites have been prepared by precipitation under hydrothermal conditions (100−200 °C).[28,29] For such single-step reactions, the interlayer cation is susceptible to replacement by hydronium ions, the coverage of the Fe^{3+} lattice sites is incomplete and powders or microcrystalline materials are obtained owing to the celerity and intractability of the precipitation reaction.[30−32] These hurdles to obtaining magnetically pure materials have been overcome with the development of redox-based hydrothermal methods.[17,19,33] Control over the precipitation of the jarosite is achieved by inserting two oxidation−reduction steps prior to jarosite precipitation

$$Fe + 2\,H^+ \rightarrow Fe^{2+} + H_2 \quad (1)$$

$$2\,Fe^{2+} + {}^1/_2\,O_2 + 2\,H^+ \rightarrow 2\,Fe^{3+} + H_2O \quad (2)$$

$$3\,Fe^{3+} + 2\,K_2SO_4 + 6\,H_2O \rightarrow KFe_3(OH)_6(SO_4)_2 + 3\,K^+ + 6\,H^+ \quad (3)$$

(28) Dutrizac, J. E. *Metallurg. Trans.* **1983**, *14B*, 531−9.
(29) Dutrizac, J. E.; Kaiman, S. *Can. Mineral.* **1976**, *14*, 151−8
(30) Dutrizac, J. E. Chen, T. T. *Can. Mineral.* **2003**, *41*, 479−88.
(31) Kubisz, J. *Mineral. Pol.* **1970**, *1*, 47−59.
(32) Kubisz, J. *Mineral. Pol.* **1971**, *2*, 51−60.
(33) Nocera, D. G.; Bartlett, B. M.; Grohol, D.; Papoutsakis, D.; Shores, M. P. *Chem. Eur. J.* **2004**, *10*, 3851−9.

Table 2. Selected Bond Distances (Å) and Bond Angles (deg) for Jarosites.

	Pb/S[a]	Ag/S	Tl/S	K/Se	Rb/Se
			Bond Distances (Å)		
A−O(2)	2.968	2.962	3.005	2.884(7)	2.906(2)
A−O(3)	2.770	2.714	2.916	2.913(7)	2.985(2)
T−O(1)	1.453(7)	1.463(8)	1.450(11)	1.611(11)	1.621(3)
T−O(2)	1.483(4)	1.477(5)	1.486(6)	1.643(7)	1.645(2)
Fe−O(2)	2.051(4)	2.041(5)	2.058(6)	2.056(6)	2.061(2)
Fe−O(3)	1.9882(17)	1.9881(19)	1.985(3)	1.987(3)	1.9855(8)
Fe···Fe distance	3.664	3.665	3.661	3.695	3.707
			Bond Angles (deg)		
O(1)−T−O(2)	109.72(16)	109.5(2)	109.9(3)	110.1(2)	110.16(7)
O(2)−T−O(2)	109.22(17)	109.4(2)	109.0(3)	108.8(2)	108.77(7)
O(2)−Fe−O(2)	180	179.999(1)	179.999(1)	179.999(1)	180.0
O(2)−Fe−O(3)	91.39(14)	91.44(16)	90.9(2)	92.5(2)	91.75(7)
O(2)−Fe−O(3)	88.61(14)	88.56(16)	89.1(2)	87.5(2)	88.25(7)
O(3)−Fe−O(3)	180	179.999(1)	179.999(1)	179.999(1)	180.0
O(3)−Fe−O(3)	91.1(2)	92.0(3)	90.4(4)	90.8(4)	90.07(12)
O(3)−Fe−O(3)	88.9(2)	88.0(3)	89.6(4)	89.2(4)	89.93(12)
Fe−O(3)−Fe	134.3(2)	134.4(3)	134.5(3)	136.8(4)	137.51(11)
Fe−O(2)−T	130.3(2)	130.3(3)	130.3(4)	126.8(4)	126.88(11)
FeO_6 tilt angle[b]	17.7	17.9	17.6	14.5	14.4

[a] Pb/S = $Pb_{0.5}Fe_3(OH)_6(SO_4)_2$, etc. [b] Tilt angle defined as (90° − (Fe···Fe−O(2)).

The overall reaction is therefore

$$3\,Fe + {}^{3}/_{4}\,O_2 + 3\,H^+ + 2\,K_2SO_4 + {}^{9}/_{2}\,H_2O \rightarrow KFe_3(OH)_6(SO_4)_2 + 3\,K^+ + 3\,H_2 \quad (4)$$

The kagomé lattice is assembled through olation of Fe^{3+} ions, which are slowly generated throughout the course of the hydrothermal process via controlled redox reactions. Moreover, unlike the rapid decrease in pH during a single-step precipitation reaction, the pH of the redox-based hydrothermal method increases. This moderation in pH is an important factor in obtaining crystalline material.

Chemical analysis of all samples used in this study gave an Fe^{3+} content of 100.0 ± 0.3% and an A^+ content of 99.5 ± 0.5%. Additionally, IR spectroscopy (Figure S1) shows no significant absorption feature at 1630 cm^{-1}, which is indicative of an H−O−H bending mode of water.[17,34] This observation speaks directly to a jarosite lattice with completely occupied Fe^{3+} sites. As we have previously discussed, protonation of OH^- by H^+ to form H_2O prevents the accrual of negative charge on kagomé layers possessing M^{3+} site vacancies. In stoichiometrically pure jarosites, as is the case reported here, water is absent in the lattice and consequently this absorption is not observed.

Structural Chemistry. Each of the jarosites crystallizes in the $R\bar{3}m$ space group. The connectivity of the heavy atoms in the asymmetric unit and the atomic labeling scheme is presented in Figure 2 for the $AgFe_3(OH)_6(SO_4)_2$ exemplar. The asymmetric unit consists of the iron atom, the oxygen of the hydroxide bridge, the central atom (sulfur or selenium) of the capping group and two of its oxygens (the unique apical oxygen and one oxygen of the pyramidal base of the capping group, as projected over the 3-fold axis). The consistency of the asymmetric unit is an especially noteworthy observation for $Pb_{0.5}Fe_3(OH)_6(SO_4)_2$, whose structure was first predicted to display Pb^{2+} residency in alternating interlayers in order to maintain charge neutrality.[35] Such a distribution of Pb^{2+} cations should

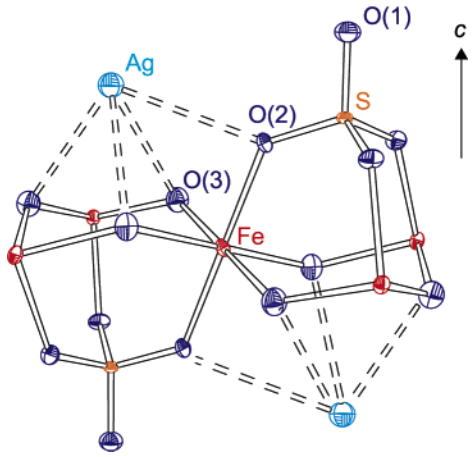

Figure 2. Basic structural unit of $AgFe_3(OH)_6(SO_4)_2$, highlighting the intralayer structure and local structure about the Fe^{3+} center. Ellipsoids are shown at 50% probability.

exhibit a *c* axis doubled superstructure on the unit cell, which has been observed (c = 34 Å) for mined samples of $Pb_{0.5}Fe_3(OH)_6(SO_4)_2$.[36] Notwithstanding, we find a *c* axis dimension of 16.795(6) Å for the stoichiometrically pure sample of $Pb_{0.5}Fe_3(OH)_6(SO_4)_2$, consistent with the known structures of all other pure jarosite compounds. The Pb^{2+} occupancy is $^1/_2$ that of a monovalent interlayer cation and Pb^{2+} is disordered along the 3-fold inversion axis. In further support of these single-crystal results, the first observed reflection in the powder diffraction pattern of $Pb_{0.5}Fe_3(OH)_6(SO_4)_2$ (Figure S2) appears at 2θ = 15.852°, corresponding to a d_{003} spacing of 5.586 Å, which is typical for the interlayer distance of jarosites; there is no diffraction feature at 11 Å corresponding to a *c*-axis doubled superstructure. The calculated cell constants from powder data yield an *a* axis of 7.310 Å and a *c* axis of 16.737 Å, in excellent agreement with single-crystal data.

As highlighted by the bond distances and angles shown in Table 2, the structure of the jarosite intralayer is remarkably similar regardless of the identity of the interlayer cation or capping group. For convenience, the metrics of the previously

(34) Power, D. A.; Rossman, G. R.; Schugar, H. J.; Gray, H. B. *J. Solid State Chem.* **1975**, *13*, 1−13.
(35) Hendricks, S. B. *Am. Mineral.* **1937**, *22*, 774−84.
(36) Szymanski, J. T. *Can. Mineral.* **1985**, *23*, 659−68.

Table 3. Direct Comparison of Sulfate- and Selenate-Capped Jarosites

	K/S[a]	K/Se	Rb/S[a]	Rb/Se
		Bond Distances (Å)		
A−O(2)	2.971(4)	2.887(8)	2.999(5)	2.906(2)
A−O(3)	2.826(4)	2.915(7)	2.902(5)	2.985(2)
T−O(1)	1.460(7)	1.614(12)	1.452(10)	1.621(3)
T−O(2)	1.481(4)	1.641(8)	1.481(5)	1.645(2)
Fe−O(2)	2.066(4)	2.056(6)	2.070(5)	2.061(2)
Fe−O(3)	1.9865(16)	1.991(3)	1.984(2)	1.9855(8)
Fe···Fe distance	3.652	3.695	3.657	3.707
		Bond Angles (deg)		
O(1)−T−O(2)	109.8(17)	110.2(2)	110.1(2)	110.16(7)
O(2)−T−O(2)	109.15(17)	108.8(2)	108.8(2)	108.77(7)
O(2)−Fe−O(2)	180	180	179.999(1)	180.0
O(2)−Fe−O(3)	91.77(13)	92.6(2)	91.04(17)	91.75(7)
O(2)−Fe−O(3)	88.23(13)	87.4(2)	88.96(17)	88.25(7)
O(3)−Fe−O(3)	180	180	179.999(1)	180.0
O(3)−Fe−O(3)	90.5(2)	90.4(4)	90.1(3)	90.07(12)
O(3)−Fe−O(3)	89.5(2)	89.6(4)	89.9(3)	89.93(12)
Fe−O(3)−Fe	133.6(2)	136.3(4)	134.4(3)	137.51(11)
Fe−O(2)−T	130.0(2)	126.9(4)	130.5(3)	126.88(11)
FeO_6 tilt angle	17.4	14.5	17.5	14.4

[a] Data taken from ref 19.

solved structures of $KFe_3(OH)_6(SO_4)_2$ and $RbFe_3(OH)_6(SO_4)_2$ have been provided (Table 3) for direct comparison to their selenate analogues now described here. Only slight structural disparities in jarosite intralayers arise as a result of differing SO_4^{2-} and SeO_4^{2-} anions, which cap the Fe_3 triangular unit of the kagomé lattice with the basal plane of the TO_4^{2-} tetrahedron. The surface area of the basal plane for SO_4^{2-} is 3.28 Å^2 vs 3.69 Å^2 for SeO_4^{2-}. The larger surface area of the latter capping anion arises from the longer T−O bond length (d_{avg}(S−O) = 1.46 Å, d_{avg}(Se−O) = 1.64 Å). The expanded SeO_4^{2-} polyhedron is conveyed to the $Fe_3(\mu\text{-}OH)_3$ triangle that it caps, though not as much as might be expected owing to a constricted Fe−O(2)−Se bond angle (∠Fe−O(2)−Se = 130.4 vs ∠Fe−O(2)−S = 126.3). The Fe···Fe distance of the selenate jarosites is slightly elongated, producing an expanded Fe−O(3)−Fe angle (134.2° for sulfate vs 137.1° for selenate). The pyramidal base of the TO_4^{2-} cap is also manifested in the metric of the FeO_6 pseudo-octahedra, which is highlighted in Figure 3 by the red outline. All Fe atoms of a triangle in the same kagomé plane must be normal to the *c* axis as crystallographically imposed by the unique Fe atom in the $R\bar{3}m$ space group. As shown in Figure 3, however, the FeO_6 pseudo-octahedra tilt to produce corrugated kagomé layers. The angle of the Fe−O(2) bond from the *c* axis provides a convenient marker of the tilt angle, which we define as {90° − [Fe···Fe−O(2)]}. The tilt angle of ∼17° for sulfate-capped jarosites is slightly larger than the ∼14° tilt angle observed in selenate-capped jarosites.

Outside of the minor structural differences arising from the different capping groups, the rigidity of the jarosite structure is noteworthy, especially for the Pb^{2+} compound. Kintoreite, $PbFe_3(OH,H_2O)_6(PO_4)_2$, a structural analogue to $Pb_{0.5}Fe_3(OH)_6(SO_4)_2$, has distorted PbO_{12} icosahedra that are ascribed to arise from the inert *s*-pair effect.[37] The Pb−O(2) distances in kintoreite range from 2.6 to 3.3 Å and the Pb−O(3) distances range from 2.6 to 3.0 Å. We observe no such distortion in jarosites, and observe single-valued Pb−O(2) and Pb−O(3) distances of 2.97 and 2.78 Å respectively; these values are consistent with those observed for jarosite with interlayer alkali metal A^+ cations. Furthermore, we see no evidence of an inert *s*-pair effect in the structure of Tl^+ analogue, which also exhibits Tl−O distances that are in line with jarosite layers occupied by alkali metal cations. Of course, one significant structural difference among the jarosites is the *c* dimension of the unit cell, which monotonically tracks the size of the intralayer cation.

(37) Kharisun; Taylor, M. R.; Bevan, D. J. M. *Mineral. Mag.* **1997**, *61*, 123−9.

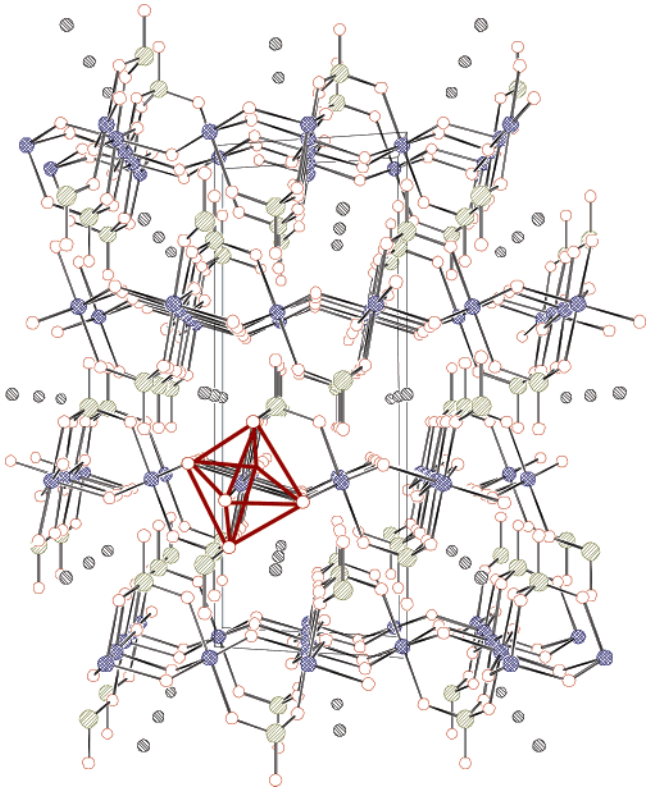

Figure 3. Packing diagram of jarosite, viewed along [110]. Note that all Fe atoms within a kagomé layer lie within a plane normal to the *c* axis. Note that the FeO_6 elongated octahedron is tilted approximately 17° from the crystallographic *c* axis. One elongated, tilted FeO_6 octahedron is highlighted.

Magnetism. The temperature and field dependence of the dc and ac susceptibility of iron jarosites was examined. Figure 4a displays the temperature dependence of the zero field-cooled (ZFC) molar susceptibilities for $AgFe_3(OH)_6(SO_4)_2$, which is representative of the other jarosites examined in this study (see Figure S3). Measurements were performed under an applied measuring field, H_m = 100 Oe. We observe a maximum in χ_m at T_N; Table 4 lists T_N values for the various jarosite derivatives. The single, frequency-independent maximum in the ac susceptibility shown for $AgFe_3(OH)_6(SO_4)_2$ in Figure 4b confirms that T_N is indeed a primary ordering event and precludes spin-glass behavior.

The susceptibility follows the Curie−Weiss law $\chi = C/(T - \Theta_{CW})$ at high temperatures. A fit of the measured susceptibilities between 150 K < *T* < 300 K yields Weiss temperatures and Curie constants listed in Table 4. For completeness, Θ_{CW} and *C* are also presented for the previously prepared jarosites possessing alkali metal cations. Extraction of the effective moment, μ_{eff}, and the nearest-neighbor exchange coupling, *J*, from these values is problematic in the case of jarosites because $T_N \ll \Theta_{CW}$. Harris et al. have addressed this issue by taking a high temperature expansion of the susceptibility for antiferromagnetically coupled spins in a kagomé lattice.[8] The analysis

Table 4. Magnetic Data for Pure Jarosites

	T_N (K)	Θ_{CW} (K)[a]	f[b]	C_m (emu·K·mol^{-1})	μ_{eff} (BM)	J[c] (cm^{-1})	d_{003} (Å)	Fe–O–Fe (deg)	tilt angle (deg)
$NaFe_3(OH)_6(SO_4)_2$	61.7	−825	13.5	5.91	6.49	32.8	5.535(10)	134.0(2)	17.6(3)
$KFe_3(OH)_6(SO_4)_2$	65.4	−828	12.7	5.77	6.41	32.9	5.728(2)	133.6(2)	17.4(3)
$RbFe_3(OH)_6(SO_4)_2$	64.4	−829	12.9	5.82	6.44	32.9	5.856(3)	134.4(3)	17.5(3)
$TlFe_3(OH)_6(SO_4)_2$	63.4	−813	12.8	6.03	6.55	32.3	5.870(2)	134.4(4)	17.6(4)
$AgFe_3(OH)_6(SO_4)_2$	59.7	−803	13.5	5.06	6.00	31.9	5.498(3)	134.0(3)	17.9(3)
$Pb_{0.5}Fe_3(OH)_6(SO_4)_2$	56.4	−832	14.8	4.38	5.58	33.1	5.598(6)	134.1(3)	17.7(3)
$KFe_3(OH)_6(SeO_4)_2$	66.5	−801	12.0	5.63	6.33	31.8	5.832(3)	130.5(3)	14.5(3)
$RbFe_3(OH)_6(SeO_4)_2$	65.1	−835	12.8	5.40	6.20	33.2	5.934(5)	137.51(11)	14.4(11)

[a] Θ_{CW} = from Curie−Weiss fit. [b] Frustration parameter defined as $f = |\Theta_{CW}|/T_N$. [c] μ_{eff} and J corrected by high-temperature expansion method as described in ref 8.

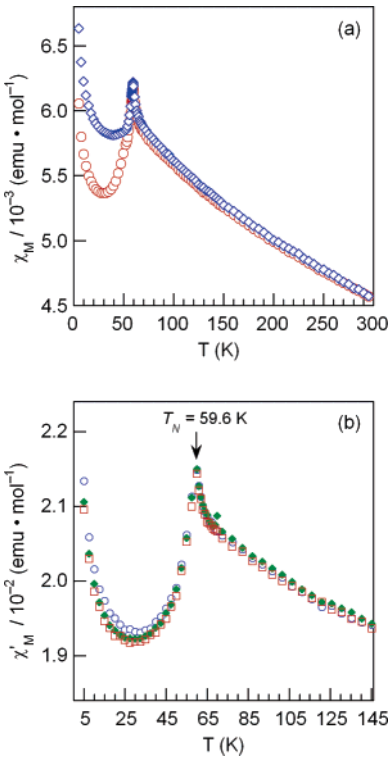

Figure 4. (a) FC and ZFC susceptibilities for $AgFe_3(OH)_6(SO_4)_2$. Both measurements were performed under a 100 Oe measuring field. For the FC measurement, the cooling field was also 100 Oe. (b) Temperature dependence on the ac susceptibility of $AgFe_3(OH)_6(SO_4)_2$ measured under an ac field, $H_{ac} = H_o \sin(2\pi ft)$ for $H_o = 3$ Oe and $f = 2$ Hz (○), 20 Hz (△), and 200 Hz (□).

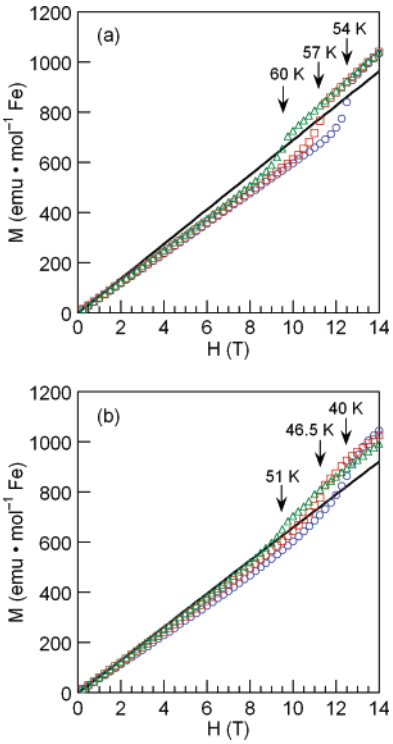

Figure 5. Magnetization curve of (a) powdered $RbFe_3(OH)_6(SO_4)_2$ at 54 K (○), 57 K (□), and 60 K (△) and of (b) powdered $Pb_{0.5}Fe_3(OH)_6(SO_4)_2$ at 40 K (○), 46.5 K (□), and 51 K (△). The solid line shows linear behavior of $M(H)$ above T_N. The labeled arrows represent the abscissa of the critical field, defined as the maximum of $(dM/dH)|_T$, which is determined from the maximum in the plots of Figure S4.

corrects the Curie and Weiss constants obtained from the result of standard mean-field theory by factors of 9/8 and 3/2, respectively

$$C = (^9/_8)[N\mu_{eff}{}^2/3k_B] \quad (5)$$

$$\Theta_{CW} = (^3/_2)[zJS(S+1)/3k_B] \quad (6)$$

where N is Avogadro's number and z is the number of nearest-neighbor spins. Applying these correction factors yields the values of μ_{eff} and J shown in Table 4 for the complete series of pure jarosites. The μ_{eff} are close to the spin-only value of 5.92 μ_B for Fe^{3+}.

To investigate further the ordering mechanism in jarosites, the field-dependent magnetization was characterized. Figure 5 shows the M vs H plots for rubidium- and plumbo-jarosites. The magnetization increases linearly when measurements are performed above T_N; this behavior is consistent with paramagnetism above the ordering temperature. As the temperature is lowered below T_N, the magnetization is observed to abruptly change at a critical field, H_c, which we define as the field at which $(dM/dH)|_T$ is a maximum. The critical fields are determined from $(dM/dH)|_T$ plots of Figure S4 and indicated by the arrows on the plots of Figure 5. The increase in magnetization is consistent with the development of a ferromagnetic moment at H_c. Below $T = 49$ K in $RbFe_3(OH)_6(SO_4)_2$ and below $T = 30$ K in $Pb_{0.5}Fe_3(OH)_6(SO_4)_2$, the critical field becomes larger than the instrument limit of 14 T and therefore a saturation H_c cannot be precisely obtained. Nevertheless, extrapolation of H_c to $T = 0$ using a power function $a + b|T - T_N|^c$ gives a saturation field of 24.3 T for rubidium jarosite and 17.3 T for $Pb_{0.5}Fe_3(OH)_6(SO_4)_2$. Also from the $M(H)$ plot, we measure ΔM, the difference in the y-intercept of the linear fits of $M(H)$ above and below H_c. Figure 6 shows the temperature dependence of H_c and ΔM. Extrapolation of ΔM to $T = 0$ gives a saturation deviation of 0.0743 μ_B for $RbFe_3(OH)_6(SO_4)_2$ and 0.0794 μ_B for $Pb_{0.5}Fe_3(OH)_6(SO_4)_2$.

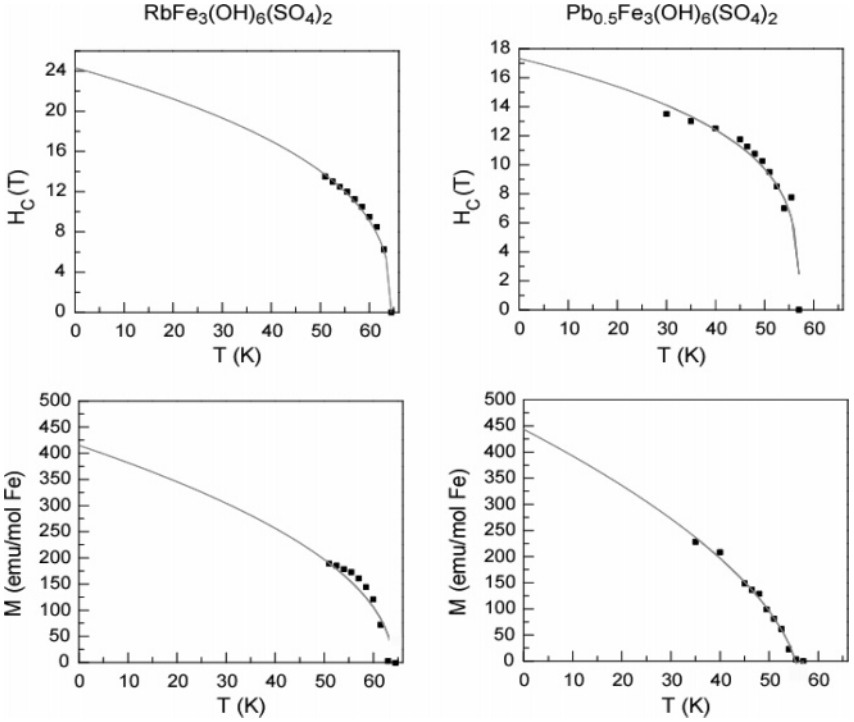

Figure 6. Temperature dependence of the critical field and magnetization difference in rubidium jarosite and $Pb_{0.5}Fe_3(OH)_6(SO_4)_2$. The data are fit to a power law function to extrapolate H_c and ΔM values at $T = 0$.

Chart 1

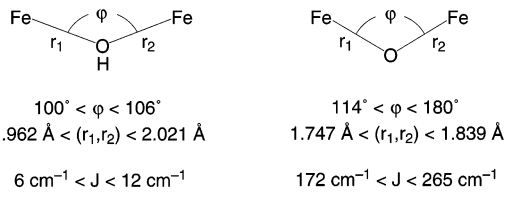

Discussion

The basic magnetic element composing the spin frustrated lattice of jarosite is the $Fe^{III}_3(\mu\text{-OH})_3$ triangle. The primary magnetic interaction occurs between nearest-neighbor Fe^{3+} ions via a bridging hydroxide. Chart 1 summarizes this exchange interaction for 6 high spin $Fe^{III}(\mu\text{-OH})Fe^{III}$ binuclear species[38] and 32 high spin $Fe^{III}(\mu\text{-O})Fe^{III}$ binuclear species.[39] All stereoelectronic models,[40] including the original orbital treatments of Goodenough[41] and Kanamori,[42] identify the predominant superexchange pathway to be comprised of metal $d_{x^2-y^2}$ orbitals and the p orbitals of the bridging oxide or hydroxide. Accordingly, J depends on the Fe−O distances r_1 and r_2 as well as on the Fe−O−Fe bridging angle, φ.[43,44] Jarosites possess values of (r_1, r_2) and φ that are midrange to those of $Fe^{III}(\mu\text{-OH})Fe^{III}$ and of $Fe^{III}(\mu\text{-O})Fe^{III}$, respectively. In accordance with this intermediate structural behavior, the observed $J \sim -30$ cm^{-1} for jarosites is greater than that observed for μ-OH bimetallic compounds (−5 to −11 cm^{-1}) but smaller than μ-O di-iron compounds (−160 to −265 cm^{-1}). As shown in Figure 7,

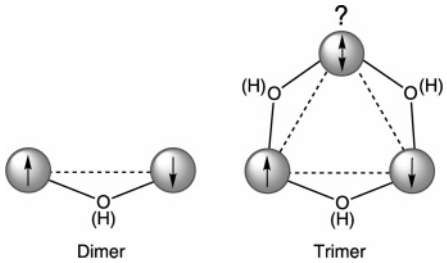

Figure 7. Antiferromagnetic spin arrangement in molecular dimers and trimers of iron. The antiferromagnetic coupling is easily achieved in dimers by the antiparallel pairing of spins on the individual iron centers. The ground-state magnetic structure of trimers cannot be satisfied by antiparallel spin pairing; the frustrated spin is indicated by the double-headed arrow.

whereas an ordered antiferromagnetic state is easily achieved for the dimers of Chart 1, an antiparallel spin arrangement is frustrated by the geometry imposed by a triangle. The addition of a third spin to the dimer structure gives rise to the complicating situation that only two of the three antiferromagnetic spin pairings can be simultaneously satisfied.

The presence of spin frustration has been sought at the molecular level in trimers of copper,[25,26,45−54] iron[55−61] and

(38) Weihe, H.; Güdel, H. U. *J. Am. Chem. Soc.* **1997**, *119*, 6539−43.
(39) Werner, R.; Ostrovsky, S.; Griesar, K.; Haase, W. *Inorg. Chim. Acta* **2001**, *326*, 78−88.
(40) Kahn, O. *Molecular Magnetism*; VCH: New York, 1993.
(41) Goodenough, J. B. *J. Phys. Chem. Solids* **1958**, *6*, 287−97.
(42) Kanamori, J. *J. Phys. Chem. Solids* **1959**, *10*, 87−98.
(43) Atanasov, M.; Angelov, S. *Chem. Phys.* **1991**, *150*, 383−93.
(44) Weihe, H.; Guedel, H. U. *J. Am. Chem. Soc.* **1998**, *120*, 2870−9.
(45) Beckett, R.; Colton, R.; Hoskins, B. F.; Martin, R. L.; Vince, D. G. *Aust. J. Chem.* **1969**, *22*, 2527−33.
(46) Butcher, R. J.; O′Connor, C. J.; Sinn, E. *Inorg. Chem.* **1981**, *20*, 537−45.
(47) Kwiatkowski, M.; Kwiatkowski, E.; Olechnowicz, A.; Ho, D. M.; Deutsch, E. *Inorg. Chim. Acta* **1988**, *150*, 65−73.
(48) Chaudhuri, P.; Karpenstein, I.; Winter, M.; Butzlaff, C.; Bill, E.; Trautwein, A. X.; Flörke, U.; Haupt, H.-J. *J. Chem. Soc., Chem. Commun*. **1992**, 321−2.
(49) Colacio, E.; Dominguezz-Vera, J. M.; Escuer, A.; Klinga, M.; Kiverkaes, R.; Romerosa, A. *J. Chem. Soc., Dalton Trans.* **1995**, 343−8.
(50) Ferrer, S.; Haasnoot, J. G.; Reedijk, J.; Müller, E.; Biagini Cingi, M.; Lanfranchi, M.; Manotti Lanfredi, A. M.; Ribas, J. *Inorg. Chem.* **2000**, *39*, 1859−67.
(51) Clérac, R.; Cotton, F. A.; Dunbar, K. R.; Hillard, E. A.; Petrukhina, M. A.; Smuckler, B. W. *C. R. Acad. Sci., Ser. IIc: Chim.* **2001**, *4*, 315−9.
(52) Ferrer, S.; Lloret, F.; Bertomeu, I.; Alzuet, G.; Borrás, J.; García-Granda, S.; Liu-González, M.; Haasnoot, J. G. *Inorg. Chem.* **2002**, *41*, 5821−30.
(53) Cage, B.; Cotton, F. A.; Dalal, N. S.; Hillard, E. A.; Rakvin, B.; Ramsey, C. M. *J. Am. Chem. Soc.* **2003**, *125*, 5270−1.

chromium.[62−62] However, magnetism characteristic of spin frustration is not typically obtained. Geometric distortion of the antiferromagnetic ground-state eradicates spin frustration by allowing a 2 (antiferromagnetic) + 1 (unpaired) spin system to be achieved.[23,65] Even when the triangles exhibit perfect 3-fold symmetry at room temperature, as is the case for the Fe_3 cluster mineral α-metavoltine,[66] and molecular triangles of iron[23,58−61] and copper,[23,25,27] low symmetry distortions prevail at low temperature and spin frustration is alleviated.

Such magnetic Jahn−Teller distortions are minimized when triangles are catenated into the extended plaquette of a kagomé lattice. The X-ray crystal data reproduced in Tables 2 and 3 show the $AFe_3(OH)_6(TO_4)_2$ jarosites to possess an undistorted triangular lattice. The spin frustration within this perfect triangular lattice is evident from the difference between the observed transition temperature, T_N, and the expected ordering temperature, given by Θ_{CW}. Because frustration inhibits the tendency for spins to order, T_N will be suppressed relative to Θ_{CW}. Ramirez has provided a measure for spin frustration by defining $f = \Theta_{CW}/T_N$, with values of $f > 10$ signifying a strong effect.[1] As is evident from the values of f in Table 4, jarosites exceed this criterion for strong spin frustration.

Spin frustration confines the localized magnetic moments on the Fe^{3+} ions composing the kagomé lattice to a 2-D plane.[67−69] For systems displaying magnetic dimensionality that is less than 3, long-range ordering (LRO) should not be observed;[3,5,6,8] yet jarosites clearly exhibit a LRO that occurs without symmetry lowering of the lattice. Recent theoretical work has suggested that the 2-D constraint induced by spin frustration in jarosites may be lifted via the antisymmetric exchange introduced by Dzyaloshinsky[70] and Moriya.[71] The DM interaction, which adds the term

$$\sum_{i \cdot j} \vec{D}(\vec{S}_i \times \vec{S}_j) \qquad (7)$$

to the spin Hamiltonian may prevail if there is no inversion center between magnetic ions. In the case of jarosites, the inversion center between Fe^{3+} ions is abolished by the tilting of the FeO_6 octahedra, leading to the corrugated layers shown in Figure 3. $\vec{D}_{ij}$ is the DM vector given by

$$\vec{D}_{ij} \propto \frac{\lambda t_{ij}^2}{\Delta U} \qquad (8)$$

where λ is the spin−orbit coupling, t_{ij} and U are the hopping and Coulomb integrals, respectively, and Δ is the crystal-field splitting for the magnetic Fe^{3+} ion within the local tetragonal crystal field of the FeO_6 coordination environment.

Within a framework of a DM interpretation for LRO, the consistency of T_N in jarosites possessing different interlayer cations and capping groups can now be understood. The basic magnetic element from which the DM interaction arises, the $Fe^{III}_3(\mu\text{-}OH)_3$ triangle, exhibits remarkable structural integrity within the jarosite intralayer. Chemical modification of the interlayer capping group or interlayer cation does little to perturb the structure of the jarosite intralayer. The inability of the former to affect intralayer structure is particularly surprising. The FeO_6 octahedra of individual triangles tilt inward owing to a mismatch between the areas of the $Fe^{III}_3(\mu\text{-}OH)_3$ intralayer triangles and basal planes of the TO_4^{2-} capping groups. One might assume that increases in area of the TO_4^{2-} basal plane would be conveyed to the intralayer triangle. However, comparison of the SO_4^{2-} and SeO_4^{2-} structures presented here show this assumption to be incorrect. The capping group distorts to preserve the structure of the of the $Fe^{III}_3(\mu\text{-}OH)_3$ triangles. These results show that it is the Fe−O−Fe linkage that is the primary determinant of the structure of the iron jarosites. With invariant metrics for the bond lengths and angles of the $Fe^{III}_3(\mu\text{-}OH)_3$ triangles, $\mathbf{D}_{ij}$ should be similar for the Fe^{3+} jarosites. This contention is supported by the consistency of T_N and J for the jarosites listed in Table 4.

The DM interaction is predicted to cause the spins on each $Fe^{III}_3(\mu\text{-}OH)_3$ triangle in the jarosite to form an umbrella structure of ferromagnetically aligned spins within each kagomé plane. The observation of T_N suggests that the ferromagnetic moments within a plane couple antiferromagnetically between layers as represented in Figure 8. The field magnetization data shown in Figure 6 provide direct and unambiguous evidence for such ferromagnetic spin canting in kagomé intralayers. As depicted in Figure 8, only the antiferromagnetic spin structure is observed below the critical field H_c. When H_c is exceeded, a nonlinear increase in M vs. H is observed as the spins begin to align with the applied field. The result is consistent with the external field overwhelming the antiferromagnetic coupling of canted spins between layers, causing a ferromagnetic alignment above H_c. Single-crystal studies reveal that a ferromagnetic component develops perpendicular to the jarosite layers, and inelastic neutron scattering studies show a doubling of the magnetic unit cell, as expected for antiferromagentically stacked

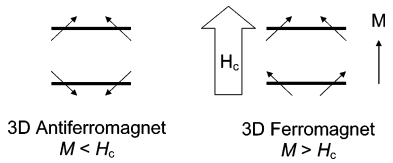

Figure 8. Field-dependent behavior of antiferromagnetically coupled layers of canted spins by the application of a strong critical field, H_c. Below H_c (left), only antiferromagnetism is observed. Above H_c (right), ferromagnetic ordering results from the alignment of the canted spins between layers.

(54) Liu, X.; de Miranda, M. P.; McInnes, E. J. L.; Kilner, C. A.; Halcrow, M. A. *Dalton Trans*. **2004**, 59−64.
(55) Rakitin, Yu. V.; Yablokov, Yu. V.; Zelentsov, V. V. *J. Magn. Reson*. **1981**, *43*, 288−301.
(56) Zheng, H.; Zang, Y.; Dong, Y.; Young, V. G.; Que, L., Jr. *J. Am. Chem. Soc.* **1999**, *121*, 2226−35.
(57) Raptopoulou, C. P.; Tangoulis, V.; Psycharis, V. *Inorg. Chem.* **2000**, *39*, 4452−9.
(58) Blake, A. B.; Frazer, L. R. *J. Chem. Soc., Dalton Trans.* **1975**, 193−7.
(59) Cannon, R. D.; Jayasooriya, U. A.; Wu, R.; Arapkoske, S. K.; Stirde, J. A.; Nielsen, O. F.; White, R. P.; Kearley, G. J.; Summerfield, D. *J. Am. Chem. Soc.* **1994**, *116*, 11869−74.
(60) Sowrey, F. E.; Tilford, C.; Wocaldo, S.; Anson, C. E.; Powell, A. K.; Bennington, S. M.; Montfrooij, W.; Jayasooriya, U. A.; Cannon, R. D. *J. Chem. Soc., Dalton Trans.* **2001**, 862−6.
(61) Hibbs, W.; van Koningsbruggen, P. J.; Arif, A. M.; Shum, W. W.; Miller, J. S. *Inorg. Chem.* **2003**, *42*, 5645−53.
(62) Wucher, J.; Gijisman, H. M. *Physica* **1954**, *20*, 361−6.
(63) Nishimura, H.; Date, M. *J. Phys. Soc. Jpn*. **1985**, *54*, 395−9.
(64) Cannon, R. D.; Jayasorriya, U. A.; Sowrey, F. E.; Tilford, C.; Little, A.; Bourke, J. P.; Rogers, R. D.; Vincent, J. B.; Kearley, G. J. *Inorg. Chem.* **1998**, *37*, 5675−7.
(65) Murao, T. *Phys. Lett.* **1974**, *49A*, 33−5.
(66) Furrer, A.; Güdel, H. U. *Helv. Phys. Acta* **1977**, *50*, 439−46.
(67) Schiffer, P.; Ramirez, A. P. *Comments Condens. Matter Phys.* **1996**, *18*, 21−50.
(68) Wills, A. S. *Can. J. Phys.* **2001**, *79*, 1501−10.
(69) Harrison, A. *J. Phys: Condens. Matter* **2004**, *16*, S553−72.
(70) Dzyaloshinksy, I. *J. Phys. Chem. Solids* **1958**, *4*, 241−55.
(71) Moriya, T. *Phys. Rev.* **1960**, *120*, 91−8.

layers of canted spins.[72] Such behavior has been observed in the square-lattice of the antiferromagnet La_2CuO_4[73] for which the DM interaction does indeed result in weak ferromagnetism.[74]

We can estimate both the spin canting angle, η, and the interlayer component to the coupling constant, J_z, following the methods of LaCroix et al. η is geometrically defined as $\sin^{-1}(\Delta M/M)$, where ΔM is the difference in the linear regime of the magnetization above and below H_c (see Figure 5) and M is the spin-only value of 5.92 μ_B for $S = 5/2$ Fe^{3+}. The magnetization curves of $RbFe_3(OH)_6(SO_4)_2$ and $Pb_{0.5}Fe_3(OH)_6(SO_4)_2$ are sufficiently linear above H_c that reliable estimates of ΔM may be ascertained; we estimate $\eta = 0.719°$ and 0.769°, respectively. J_z may be determined from

$$J_z = \frac{\Delta M(0)\, H_c(0)}{z\, S^2} \qquad (9)$$

where $\Delta M(0)$ and $H_c(0)$ are the magnetization and critical field at $T = 0$. Figure 6 provides extrapolations to $T = 0$ for ΔM and H_c. Using eq 9, we obtain $J_z = 0.034$ cm^{-1} for $RbFe_3(OH)_6(SO_4)_2$ and 0.020 cm^{-1} for $Pb_{0.5}Fe_3(OH)_6(SO_4)_2$. We note that the extrapolation was made using a conventional power law, which overestimates the zero temperature values of $\Delta M(0)$ and of $H_c(0)$. Despite the overestimation, we see that the interlayer coupling is at least 3 orders of magnitude smaller than the coupling deduced from eq 6, which provides the exchange interaction for nearest-neighbor (NN) moments within the kagomé plane. The disparity between J_z and J_{NN} attests to high two-dimensional nature of the magnetism in jarosites. Even though J_z is small, it can give rise to sizable T_N when the correlation length of the canted spins is large. For instance, experimental fitting of the temperature dependence of the in-plane and out-of-plane susceptibility in La_2CuO_4 using modified Landau theory[75] shows that the T_N of 216 K results from a J_z of only 8×10^{-3} cm^{-1}, but propagated over a large correlation length of $\xi = 768$ Å.[76] Since the correlation length is exponentially related to the exchange interaction, the large Θ_{CW}s of jarosites suggest that the small out-of-plane component brought about by the DM interaction is correlated over a long length scale, thus accounting for the appreciable T_Ns of Table 4.

Conclusions

Spin anisotropy arising from the Dzyaloshinsky−Moriya interaction provides a mechanism for ordering in triangular spin arrays. In a molecule, the DM interaction is not prevalent owing to the propensity of the triangle to distort. Conversely, in extended triangular arrays, low symmetry structural distortions are minimized and the DM interaction can emerge as the primary mechanism for ordering. Such is the case for jarosites. The placement of antiferromagnetically coupled spins onto this kagomé lattice leads to a high degree of spin frustration, forcing spins into the 2-D plane of the array. The DM interaction appears by canting spins away from the geometrically frustrated 2-D plane and LRO results. Even when the canting of the spin is small, as measured here for jarosites, a pronounced ordering temperature can be observed owing to long correlation lengths for a spin-frustrated kagomé lattice.

The LRO arising from the DM interaction in jarosites obscures the disordered spin ground states that are expected to result from spin frustration. The results reported here show that the DM interaction will be difficult to suppress or eliminate by chemical modification of the jarosite lattice owing to the structural rigidity of the $Fe^{III}_3(\mu\text{-}OH)_3$ triangles. For this reason, an imperative is provided for the synthesis of new kagomé lattices. Those possessing $S = {}^1/_2$ magnetic ions are especially intriguing because: (1) the magnitude of the DM interaction will be minimized with decreasing S and (2) many theoretical investigations suggest that a kagomé lattice with $S = {}^1/_2$ magnetic ions is the ideal venue in which a quantum spin liquid phase may be manifested.[8−10,77,78] To this end, Cu^{2+} kagomé lattices are current targets of synthetic investigation.

Acknowledgment. We thank Drs. Young S. Lee, Dimitris Papoutsakis, Daniel Grohol, Matthew P. Shores and Fangcheng Chou for helpful discussions on magnetism aspects of this work, Mr. Fisher O. Ven for aiding the development of synthetic methods, and Dr. William M. Davis, Mr. David R. Manke and Dr. Peter Mueller for assistance with X-ray structure determinations. This work was supported in part by the MRSEC Program of the National Science Foundation under award number DMR 98-08941, and by a Sigma-Xi Grants-in-Aid Award to B.M.B. B.M.B. also thanks the National Science Foundation Graduate Research Fellowship Program for support.

Supporting Information Available: FTIR spectra, the ZFC magnetic susceptibilities, the powder X-ray diffraction pattern of $Pb_{0.5}Fe_3(OH)_6(SO_4)_2$, $(dM/dH)|_T$ plots of $RbFe_3(OH)_6(SO_4)_2$ and $Pb_{0.5}Fe_3(OH)_6(SO_4)_2$, and the crystallographic tables and CIF files for the newly prepared jarosites are presented. This material is available free of charge via the Internet at http://pubs.acs.org.

JA050205D

(72) Grohol, D.; Matan, K.; Cho, J. H.; Lee, S. H.; Lynn, J. W.; Nocera, D. G.; Lee, Y. S. *Nature Mater.* **2005**, *4*, 323−8.
(73) Wells, B. O.; Birgeneau, R. J.; Chou, F. C.; Endoh, Y.; Johnston, D. C.; Kastner, M. A.; Lee, Y. S.; Shirane, G.; Tranquada, J. M.; Yamada, K. *Z. Phys. B: Condens. Matter* **1996**, *100*, 535−45.
(74) Thio, T.; Thurston, T. R.; Preyer, N. W.; Picone, P. J.; Kastner, M. A.; Jessen, H. P.; Gabbe, D. R.; Chen, C. Y.; Birgeneau, R. J.; Aharony, A. *Phys. Rev. B* **1988**, *38*, 905−8.
(75) Morrish, A. H. *The Physical Principles of Magnetism*; IEEE Press: New York, 2001.
(76) Uchinokura, K.; Ino, T.; Terasaki, I.; Tsukada, I. *Physica B* **1995**, *205*, 234−48.
(77) Waldtmann, C.; Everts, H.-U.; Bernu, B.; Lhuillier, C.; Sindzingre, P.; Lecheminant P.; Pierre, L. *Eur. Phys. J. B* **1998**, *2*, 501−7.
(78) Hastings, M. B. *Phys. Rev. B* **2001**, *63*, 014413/1−16.